Mitigation of Open-Circuit Voltage Losses in Perovskite Solar Cells Processed over Micrometer-Sized-Textured Si Substrates

Ahmed Farag,* Paul Fassl, Hang Hu, Thomas Feeney, Aina Quintilla, Marco A. Ruiz-Preciado, Wolfram Hempel, Dominik Bagrowski, Philipp Noack, Bianca Wattenberg, Torsten Dippell, and Ulrich W. Paetzold*

The recent development of solution-processed perovskite thin films over micrometer-sized textured silicon bottom solar cells enables tandem solar cells with power conversion efficiencies > 30%. Next to improved light harvesting, textured silicon wafers are the industrial standard. To achieve high performance, the open-circuit voltage losses that occur when fabricating perovskite solar cells over such textures need to be mitigated. This study provides a practical guideline to discriminate and address the voltage losses at the interfaces as well as in the bulk of solution-processed double cation perovskite thin films using photoluminescence quantum yield measurements. Furthermore, the origin of these losses is investigated via morphological, microstructural, and compositional analysis and present possible mitigation strategies. The guideline will be beneficial for scientists working on randomly textured surfaces and provides a deeper understanding on this timely research topic.

A. Farag, P. Fassl, H. Hu, T. Feeney, M. A. Ruiz-Preciado, U. W. Paetzold
Light Technology Institute
Karlsruhe Institute of Technology (KIT)
Engesserstrasse 13, 76131 Karlsruhe, Germany
E-mail: ahmed.farag@kit.edu; ulrich.paetzold@kit.edu
A. Farag, P. Fassl, H. Hu, M. A. Ruiz-Preciado, U. W. Paetzold
Institute of Microstructure Technology
Karlsruhe Institute of Technology (KIT)
Hermann-von-Helmholtz-Platz 1
76344 Eggenstein-Leopoldshafen, Germany
A. Quintilla
Center for Functional Nanostructures
Karlsruhe Institute of Technology (KIT)
Wolfgang-Gaede-Strasse 1a, 76131 Karlsruhe, Germany
W. Hempel, D. Bagrowski
Zentrum für Sonnenenergie- und Wasserstoff-Forschung
Baden-Württemberg (ZSW)
Meitnerstr. 1, 70563 Stuttgart, Germany
P. Noack, B. Wattenberg, T. Dippell
Singulus Technologies AG
Hanauer Landstrasse 103, D-63796 Kahl/Main, Germany

The ORCID identification number(s) for the author(s) of this article can be found under https://doi.org/10.1002/adfm.202210758.

1. Introduction

In recent years, monolithic perovskite/silicon (Si) tandem solar cells[1–18] have experienced enormous improvements in their power conversion efficiency (PCE), which makes this photovoltaic (PV) technology one of the most promising candidates to surpass the theoretical limit of a single-junction solar cell (33.7%).[19,20] Recently, a record PCE of 31.25% for monolithic two-terminal (2T) perovskite/Si tandem solar cells has been reported, which surpasses by far the record PCE of single-junction Si solar cells (26.7%).[21] Next to 2T architecture, four-terminal and monolithic three-terminal (3T) architectures are promising concepts. The latter provides the ease of fabrication of the 2T architecture while circumventing the current matching requirement that limits the range of suitable perovskite band gaps.[22–26]

In view of their wide commercial deployment, textured Si bottom solar cells are industrially more relevant compared to planar or even polished Si front surfaces for monolithic 2T or 3T perovskite/Si tandems. Moreover, they enable improved light management that is required to maximize current generation and thus essential to maximize the PCE, as demonstrated by the recently reported certified PCEs of 29.3%[27] and 31.25%.[21] Yet, while textured Si solar cells exhibit excellent light harvesting properties (light incoupling and light trapping),[2,3,11,15,28,29] controlling the morphology and quality of perovskite thin films deposited over such textured surface is challenging due to the roughness of the processing surface. Initially, vacuum deposition[7,30,31] and a hybrid 2-step process[6,32–34] have been employed to ensure a full coverage of perovskite thin films on micrometer-sized textured Si surfaces with large pyramid sizes > 2 μm, which however did not result in very high PCE due to the limited quality of the perovskite absorber. More recently, the development of smaller textures with pyramid sizes in the range of ≈0.5–2 μm has enabled successful deposition via blade coating,[35] slot-die coating,[28] and most often, spin-coating.[3,27,36–40]

The most important PV parameter reflecting the optoelectronic quality of perovskite thin films processed over textures is the open-circuit voltage (V_{OC}). To achieve highest performance for perovskite solar cells (PSCs), various interlinked open-circuit voltage losses need to be mitigated.[41–43] However, to

**ADVANCED
SCIENCE NEWS**

www.advancedsciencenews.com

**ADVANCED
FUNCTIONAL
MATERIALS**

www.afm-journal.de

date, a comprehensive study that analyses the voltage losses of solution-processed perovskite thin films over micrometer-sized pyramidal textures is missing. In this work, we present a practical guideline to discriminate these voltage losses using a set of photoluminescence quantum yield (PLQY) measurements for double cation $Cs_{0.17}FA_{0.83}PbI_{2.75}Br_{0.25}$ perovskite thin film stacks deposited over micrometer-sized textured Si substrates. We further analyze the microstructure, composition, and crystallinity of the films using time-of-flight secondary ion mass spectrometry (ToF-SIMS), glow-discharge optical emission spectroscopy (GDOES), scanning electron microscopy (SEM), atomic force microscopy (AFM), and X-ray diffraction spectroscopy (XRD). We provide a step-by-step guidance on how to address the voltage losses focusing on the following aspects: 1) we optimize the hole transport layer (HTL) to minimize non-radiative recombination at the HTL/perovskite interface; 2) we optimize and analyze the effect of (i) the dripping time of the anti-solvent and (ii) the PbI_2 excess in the precursor solution; 3) we investigate in depth the interactions of the HTL and transparent conductive oxide (TCO) with the perovskite; 4) we provide a guide to control the surface morphology using a proper perovskite precursor solution concentration and solvent ratio; and 5) we manage to reduce the detrimental voltage losses at the perovskite/C_{60} interface[44] using proper surface passivation strategies. The insights and voltage loss mitigation strategies of our study will be beneficial for researchers who process perovskites onto textured or rough surfaces in general and will help to further develop this important research direction.

2. Results and Discussion

2.1. Voltage Losses at the HTL/Perovskite Interface

Given the increase in surface area when processing over a textured as compared to a planar surface, choosing a proper HTL is critical to minimize the voltage losses at the HTL/perovskite interface. Various HTLs such as nickel oxide (NiO_x), Poly-TPD, and PTAA are widely employed in the inverted p–i–n PSC architecture.[7,35,45–57] NiO_x can be prepared at high quality using a large variety of techniques, such as spin-coating,[50,51] electrochemical deposition,[52] screen printing,[53] sputtering,[54–56] atomic layer deposition (ALD),[45,57] and e-beam evaporation.[46,47] Since the quality of the HTL plays a key role in fabricating efficient PSCs, several studies proposed methods to improve NiO_x thin film quality[48] by introducing process gasses, heating the substrate during deposition, or introducing dopants during the film formation.[50,51,58,59] In our study, we use sputtered NiO_x to assure a conformal surface coverage over the micrometer-sized pyramidal textures.[34,38] Although NiO_x-based PSCs often exhibit good long-term stability,[47,54,55] relatively high hysteresis and voltage losses due to chemical interactions between NiO_x and the perovskite film are commonly observed drawbacks when employing this HTL.[60–64] In this regard, self-assembled molecules (SAMs) have presented themselves as a very good alternative HTL for both single-junction p–i–n PSCs as well as monolithic tandem solar cells.[12,27,65] The excellent energy level alignment and suppressed non-radiative recombination losses result in a significantly higher V_{OC} and fill factor (FF) compared to other HTLs.[49,66] However,

conformally covering a micrometer-sized texture with a solution-processed ultrathin HTL remains challenging, and the exposed regions can lead to detrimental shunting paths, which consequently hinder overall performance and decrease the fabrication yield.[32,34] Combining a sputtered NiO_x layer that provides a uniform and conformal coverage with solution-processed SAMs as a double-layer HTL has demonstrated comparable or even better PCEs compared to using stand-alone SAMs for PSCs processed over planar substrates.[10,34,57,67–70]

To quantitatively analyze and compare non-radiative recombination at the HTL/perovskite interface, we performed PLQY measurements on samples prepared with either a single-layer NiO_x or a double-layer of NiO_x/2PACz as HTL. We investigate half-stacks of the PSCs consisting of indium tin oxide (ITO)/HTL/perovskite over micrometer-sized textured Si substrates without introducing a C_{60} layer on top to reliably account only for V_{OC} losses that could be attributed to the HTL/perovskite interface. For the reference stack (with NiO_x as an HTL), we measure a rather low PLQY with an average value of 0.3%. Depositing a 2PACz layer onto the sputtered NiO_x film enhances the PLQY by roughly an order of magnitude to an average value of 2.5% as shown in **Figure 1**b. Both values are comparable to a previous report by Li et al., showing that the quality of the perovskite films on our textured substrates is indeed similar to films processed on planar substrates.[70] Figure 1c highlights the superiority of the double-layer HTL with an average implied V_{OC} of 1.196 V compared to the NiO_x reference with 1.145 V (see Experimental Section for more details regarding the calculation of implied V_{OC}). The average gain of ≈50 mV is in full agreement with previously reported values for planar PSCs using the same or other double-layer HTL.[64,68,70]

To obtain the internal ideality factor (n_{id}) for the corresponding perovskite half-stacks, we perform intensity-dependent PLQY measurements and apply a fit to the calculated implied V_{OC}.[42] The NiO_x stack exhibits an ideality factor of $n_{id} = 1.74$ (Figure 1d), which is considerably reduced to $n_{id} = 1.53$ for NiO_x/2PACz. A smaller value of n_{id} toward a value of one is typically associated with a predominant bimolecular radiative and reduced trap-assisted Shockley–Read Hall recombination, resulting in higher V_{OC} and FF.[42,49,71,72] Together with the increase in absolute implied V_{OC}, we therefore attribute this trend with a reduced non-radiative recombination at the HTL/perovskite interface.[49]

2.2. Effect of Processing Parameters on Voltage Losses

Most reports on PSCs with high V_{OC} and high PCE employ multi-cation perovskite thin films processed with the anti-solvent quenching technique. The anti-solvent is required to induce prompt crystallization, which features pinhole-free perovskite thin films with crystallites that have dimensions >500 nm. In most recipes, the anti-solvent is dropped in a narrow time window between 12–20 s during the second spin-coating step, which will be referred to as "early quenching" in the following.[49,73–76] However, from cross-sectional SEM images we find that in the valleys of the pyramidal textures of the substrate there are apparent perovskite-free regions (aka. voids) for the perovskite thin films processed with early quenching (see **Figure 2**a; Figure S1a, Supporting Information).
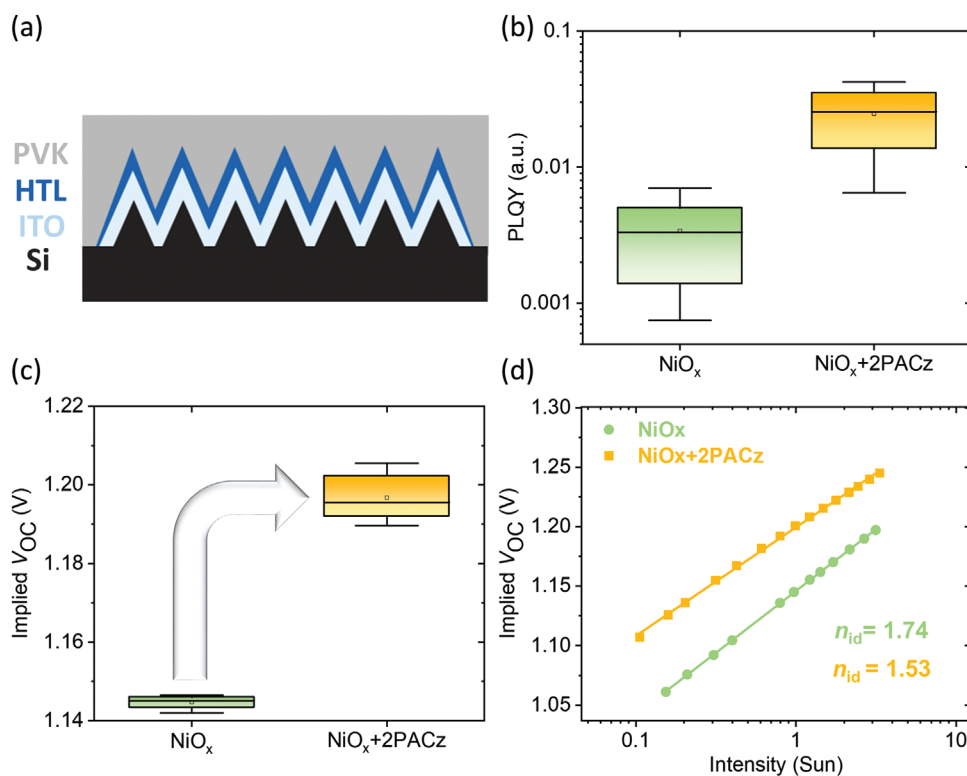
Figure 1. a) Schematic diagram of the ITO/HTL/perovskite (PVK) ($Cs_{0.17}FA_{0.83}PbI_{2.75}Br_{0.25}$) half-stack on a micrometer-sized textured Si substrate. The HTL applies for NiO_x and $NiO_x/2PACz$. b) Comparison of the photoluminescence quantum yield (PLQY) for the half-stack when the two different HTLs are used and c) the corresponding implied V_{OC}. d) Ideality factor (n_{id}) extracted from a fit to the intensity-dependent implied V_{OC}.

Chen and co-workers have reported on voids at the perovskite/substrate interface for perovskite thin films processed over planar substrates using the anti-solvent quenching technique.[77,78]

As the crystallization of the perovskite film starts at the film-air interface as a result of the solvent evaporation that occurs during the anti-solvent quenching, a solid shell starts to form
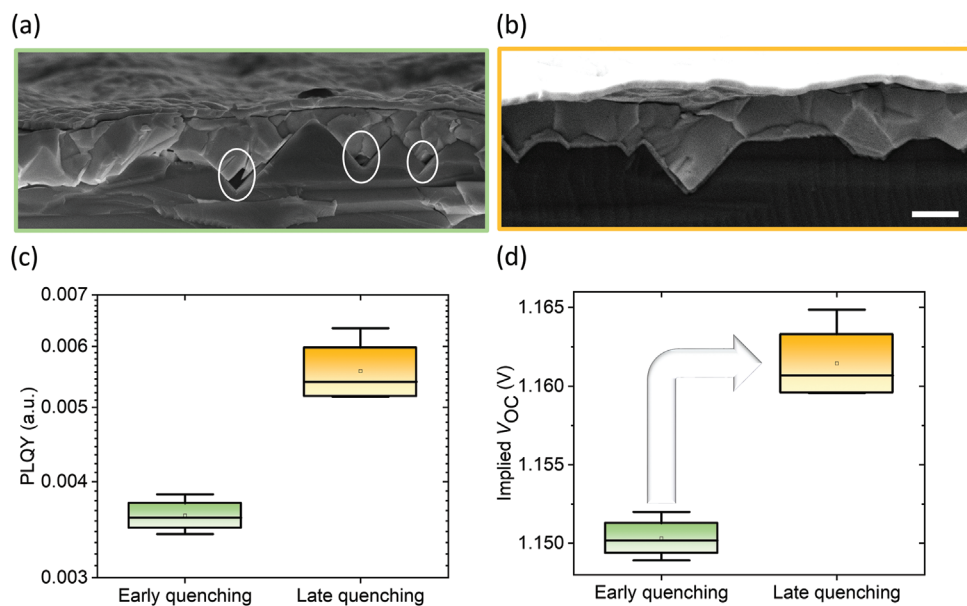

Figure 2. a,b) Cross-sectional SEM images of PSCs processed using early (12 s) and late (55 s) quenching respectively (more images can be found in Figure S1, Supporting Information), the scale bar is 1 µm. c,d) PLQY and implied V_{OC} comparison. We performed the measurements employing the half-stack ITO/NiO_x/2PACz/perovskite.

at the surface and temporarily traps wet film close to the perovskite/substrate interface. The high-boiling point dimethyl sulfoxide (DMSO) in the trapped wet film will eventually escape the film after annealing, resulting in voids near the perovskite/substrate interface due to the volume collapse.[77–79] In agreement with this hypothesis and considering the complexity of the crystallization dynamics of the perovskite thin film on top of the textured surface, which originates from three different surface types on the micrometer scale (i.e., walls, tips, and valleys), the wet film is trapped mostly in the valleys (considering a peak to valley distance of ≈1.5 μm). We note that such voids are absent if the perovskite is processed over a planar surface using early quenching as reported in our previous work.[80]

To resolve this issue and minimize the trapped DMSO volume in the pyramids valleys, we optimized the anti-solvent dropping time to 55 s, which we term "late quenching" in the following. As shown in the SEM cross-sections in Figure 2b and Figure S1b (Supporting Information), the pyramids valleys are completely filled with no voids being present. The presence of voids at the HTL (NiO_x+2PACz in our case)/perovskite interface causes imperfect contact, which reduces charge carrier extraction and, in turn, is expected to decrease the FF. Indeed, the current density-voltage (J–V) curve of a PSC fabricated using early quenching exhibits high series resistance (see Figure S2b, Supporting Information) and on average an ≈8.5% lower FF compared to PSCs fabricated using late quenching (see Figure S2c, Supporting Information). We note that additional microscale experiments such as confocal PL at short circuit or open circuit conditions could shed more light on the local variations in charge extraction, but these are beyond the scope of this work.[81,82] At the same time, we observe a gain in V_{OC} from an average of ≈0.99 to ≈1.04 V (see Figure S2d, Supporting Information). In order to understand if this enhancement only stems from enhanced charge extraction or if nonradiative is effectively reduced, we performed PLQY measurements (Figure 2c,d) and compare the trend in device V_{OC} to the implied V_{OC}. In fact, we find that early quenching results in significant losses in implied V_{OC}. This indicates that these perovskite-free regions additionally act as recombination centers that negatively impact device V_{OC}.[83,84]

To summarize, our analysis shows that late quenching, i.e., dropping the anti-solvent after 55 s instead of 12 s, provides perovskite thin films on textured Si substrates both with less voids (better morphology and enhanced charge extraction) and reduced non-radiative recombination losses (better optoelectronic quality). This highlights the importance of adapting the perovskite process parameters to the textured Si surface to minimize voltage losses and enhance the FF.

2.3. Effect of Precursor Stoichiometry on Voltage Losses

Next to non-radiative recombination losses at the perovskite/HTL interface, non-radiative recombination at defects in the bulk and grain boundaries reduce the V_{OC}. In this regard, the stoichiometry of the perovskite precursor solution and additives can influence the quality of the perovskite thin film in the bulk and at the interfaces.[85–88] More specifically, many high PCE/V_{OC} PSCs reported to date introduce excess PbI_2

into the perovskite precursor solution.[49,74,75,89] Extensive studies have been made to understand the impact of excess PbI_2 in the perovskite precursor solution on the perovskite film quality.[90–99] The role that excess PbI_2 plays in passivating the grain boundaries and interfaces leads to enhancement in the V_{OC}, FF, and photocurrent.[100–104] In addition, Yang and co-workers have shown that iodine management in formamidinium lead halides by introducing I_3^- to the dripping solution, heals defect sites and decreases the number of deep-level traps within the bulk.[105] In that regard, it has been reported that chemical interactions between NiO_x (when used as an HTL in the p–i–n architecture) and the perovskite, possibly related to $Ni^{>=3+}$ reacting with A-site cations in the perovskite precursor solution, can potentially form a defect-rich interface resulting in reduced performance and/or stability.[53,62,64,106–108] As discussed above and in other reports, the negative impacts of these interactions on the optoelectronic properties of PSCs can be strongly reduced by employing a double-layer HTL.[63] However, in case of textured substrates with a much larger surface area, the effect of the exact precursor stoichiometry on i) the strength of these interactions and ii) on crystallization behavior in general is unknown. Due to the key role that film stoichiometry, iodine deficiency, and crystallinity play on voltage losses, stability, and efficiency of PSCs,[94,95,98,109–111] we further investigate in this direction.

For multi-cation perovskite films processed over planar substrates, typically a moderate excess of PbI_2 (≈5–10%) in the precursor solution is used to achieve highest V_{OC}. Already slightly higher (or lower) amounts of excess PbI_2 can negatively affect device performance.[90,102] We find that the 1.6 м perovskite precursor solution (which is essential to provide full surface coverage over the micrometer-sized pyramidal textures as discussed in the next section) results in a high volume fraction of PbI_2 when processed over a planar Si substrates employing 10% excess PbI_2 (see XRD spectra in **Figure 3**a).[80,112] Interestingly, the PbI_2 diffraction peak intensity is strongly decreased once the perovskite thin film is processed over the textured surface compared to the planar reference. We emphasize that we used the same perovskite precursor solution and the same processing parameters for both the textured and planar Si substrates. We have also performed XRD measurements on thinner perovskite films (regardless of surface coverage) deposited onto planar and textured half-stacks using lower perovskite precursor solution concentrations (1 and 1.3 м) and obtained similar results to the 1.6 м case (see Figure S3, Supporting Information). Such a decrease in crystalline PbI_2 volume fraction has been reported before, for example for recipes using additives in the perovskite precursor solution if they tend to form complex compounds with the PbI_2 (e.g., Lewis acids and bases).[80,113–115] However, this explanation is not plausible in case only the substrate type is varied (from planar to texture). A more plausible explanation for the reduced PbI_2 volume fraction is the interaction of the perovskite with the NiO_x-based HTL.[62,106,107]

To shed light on the potential reasons for the reduced intensity of the PbI_2 peak observed for perovskite film processed over textured Si substrates we studied the elemental distribution throughout the perovskite film via GDOES depth-profiling.[116,117] As shown in Figure 3b, the expected signals from Pb, I, and Br belonging to the employed $Cs_{0.17}FA_{0.83}PbI_{2.75}Br_{0.25}$
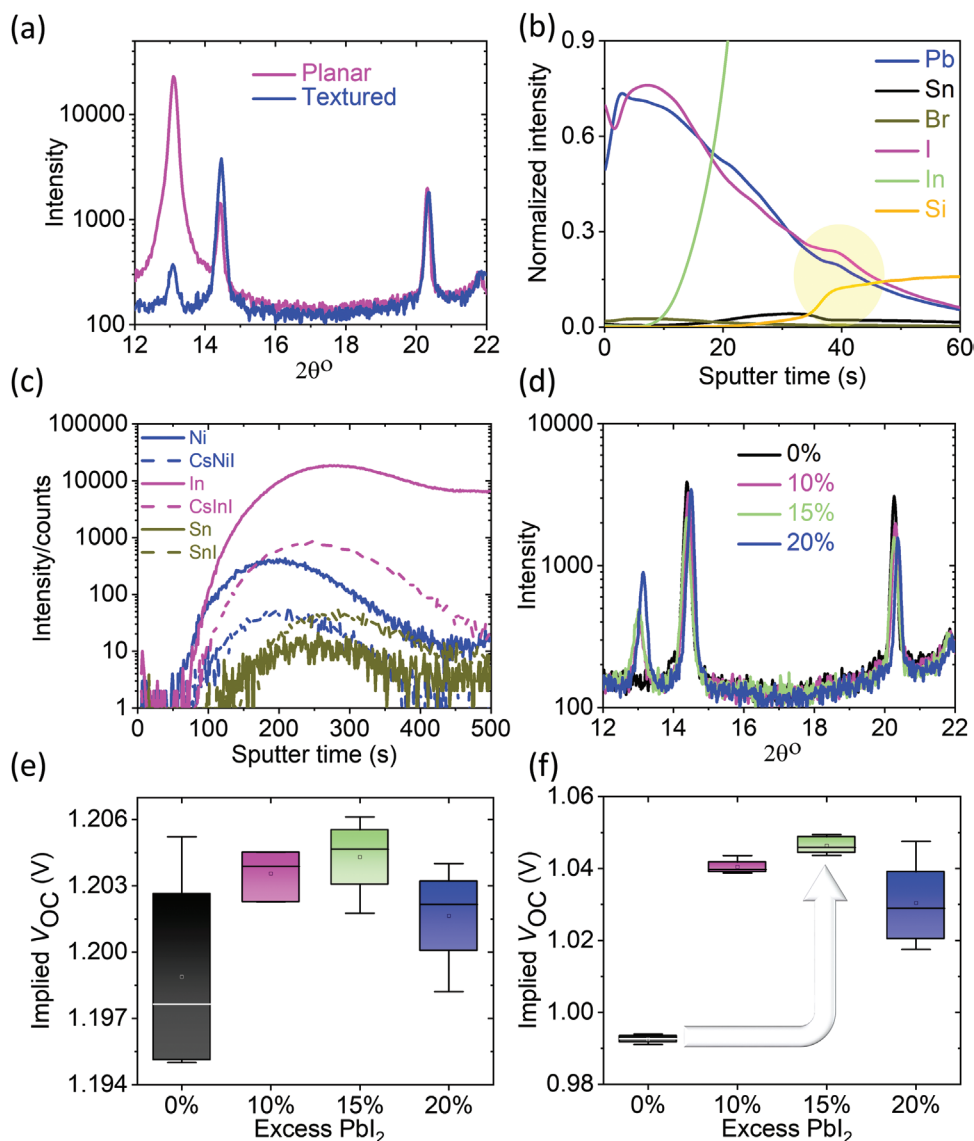
Figure 3. a) XRD spectra for perovskite films processed onto the half-stack ITO/NiO$_x$/2PACz/perovskite over textured and planar Si substrates. b) GDOES spectra for a perovskite film over the textured half-stack. c) ToF-SIMS spectra for a similar stack as in b. d) XRD spectra for perovskite films over the textured half-stack with 0, 10, 15, and 20% excess PbI$_2$. e,f) Corresponding implied V_{OC} data for the films in d, without and with C$_{60}$ respectively.

are observed at the start of sputtering, i.e., on the surface of the film. After ≈20 s sputtering, a signal from Si starts to appear, which we attribute to the time when the first pyramid tips are exposed. Only after ≈35 s, the signal from Si starts to increase considerably, attributed to the time when most of the perovskite film within the valleys has been removed. Looking specifically at the distribution of iodine as compared to the Pb signal, we find a relative increase shortly before the main Si signal starts to arise (see yellow circle). This indicates that there is more iodine within the valleys as compared to the main bulk of the perovskite film, i.e., after ≈15–25 s sputtering. Another interesting observation is that the bromine signal decreases monotonically with increasing sputtering times, indicating the bromine is mainly located at the perovskite film surface (see Figure S4 for zoom-in, Supporting Information). The relative increase in iodine close to the Si substrate indicates that

the bottom side of the perovskite film is more iodine-rich, which could be attributed to the above-discussed chemical redox interactions between A-site cations in the perovskite and NiO$_x$.[53,62,106–108] To further investigate why the bottom side of the perovskite film is iodine-rich, we use ToF-SIMS.[118–122] The depth-profiling measurement in Figure 3c using bismuth ion beam for analysis and cesium ion beam for sputtering as described in the Experimental Section (the full data set is in Figure S5, Supporting Information) shows that when a combination of sputtered NiO$_x$ and solution-processed 2PACz is used as an HTL, the iodine interacts with nickel (Ni) forming nickel iodide as represented by its cesium cluster that arises simultaneously with the Ni signal. This strengthens our hypothesis for an interaction of the iodine with the positive ions of the NiO$_x$-based HTL, in full agreement with literature regarding for similar p–i–n PSC stacks.[53,62,106,107]

**ADVANCED
SCIENCE NEWS**

www.advancedsciencenews.com

**ADVANCED
FUNCTIONAL
MATERIALS**

www.afm-journal.de

Interestingly, the discussed chemical interaction does not stop at the HTL, since we observe a similar interaction is taking place with the ITO layer underneath. Indium iodide (represented by its cesium cluster) and tin iodide signals are present simultaneously with the indium and tin signals. The indium iodide and tin iodide signals are also present when a standalone 2PACz is used as HTL (see Figure S6, Supporting Information). We also note the same interaction is taking place for perovskite films processed over planar substrates as they are deposited over the same TCO and HTL (Figure S7, Supporting Information), which indicates the consistency of the reaction mechanism. However, when processing the perovskite film over a textured surface, the interaction surface area is drastically increased due to the larger surface area of the HTL and TCO in case of a single-junction PSC, or the HTL and recombination junction in case of monolithic tandem solar cells. Hence, signal intensities are higher and start to arise earlier in the textured surface case (see comparison in Figure S8, Supporting Information). To emphasize that the interaction is rather universal, we performed energy-dispersive X-ray spectroscopy (EDX) mapping on a completely different perovskite composition [triple-cation $Cs_{0.05}MA_{0.22}FA_{0.73}Pb(I_{0.77}Br_{0.23})_3$] over a planar surface that has the same TCO (ITO) and HTL (NiO_x/2PACz). Similar to the previously discussed results, the maps indicate high iodine concentration near the HTL/perovskite interface (Figure S9, Supporting Information). Our analysis indicates the iodine consumed during the interaction with the HTL and TCO for films processed over the textured surface is high compared to the planar surface and might correlate to the drop in the PbI_2 diffraction peak in the case of depositing perovskite over the textured surface.

Due to the observed differences in the chemical interactions of the perovskite film with the NiO_x-based HTL as well as the TCO, in addition to the difference in the PbI_2 XRD peak intensity between perovskite films processed over the planar and the textured substrate, we found it necessary to revisit the typically employed 10% excess PbI_2 in the perovskite precursor solution and search for the best value for textured surfaces. For this, we performed XRD and PLQY measurements of ITO/NiO_x/2PACz/Perovskite half-stacks for four different amounts of excess PbI_2 (0%, 10%, 15%, and 20%) as shown in Figure 3d,e. The stoichiometric film does not exhibit a PbI_2 peak at all and the corresponding implied V_{OC} is ≈1.20 V. Increasing the amount of excess PbI_2 in the perovskite precursor solution correlates with the size of the PbI_2 diffraction peak intensity while the implied V_{OC} for all concentrations is only slightly higher as compared to the stoichiometric film (Figure 3e) (see comparison of the absolute PLQY in Figure S10, Supporting Information). This indicates that the optoelectronic quality of the bulk perovskite in contact with NiO_x/2PACz is not severely affected by the exact amount of excess PbI_2. As expected, the non-radiative recombination losses increase in all four cases once we introduce the C_{60} layer onto the half-stack. Interestingly, the average implied V_{OC} values still follow the same trend as without C_{60}, but the absolute differences are much larger with values of 0.992, 1.04, 1.047, and 1.029 V for excess PbI_2 of 0%, 10%, 15%, and 20%, respectively (Figure 3f). We note that the external V_{OC} data of the full device stack exhibit a comparable trend as shown in Figure S11 (Supporting Information). We conclude that 15% excess PbI_2 is favorable slightly before, but especially after introducing the electron transport layer (ETL). This emphasizes that the exact amount of excess PbI_2 not only affects the NiO_x/2PACz/perovskite interface, but also the interface toward C_{60}.

2.4. Surface Coverage and Voltage Losses

Assuring full surface coverage is necessary to prevent detrimental shunting paths caused by pyramidal tips that extend out to the surface of the perovskite thin film. When depositing a perovskite film using a 1.4 M precursor solution of a double-cation ($Cs_{0.17}$ $FA_{0.83}PbI_{2.75}Br_{0.25}$) perovskite over the micrometer-sized texture, we observe a considerable number of uncovered pyramid tips that strongly contribute to the high root mean square (RMS) roughness of ≈150 nm as indicated by the 3D representation of the AFM measurements in **Figure 4**. In case of a 1.6 M precursor solution, no tips are reaching out and the RMS roughness
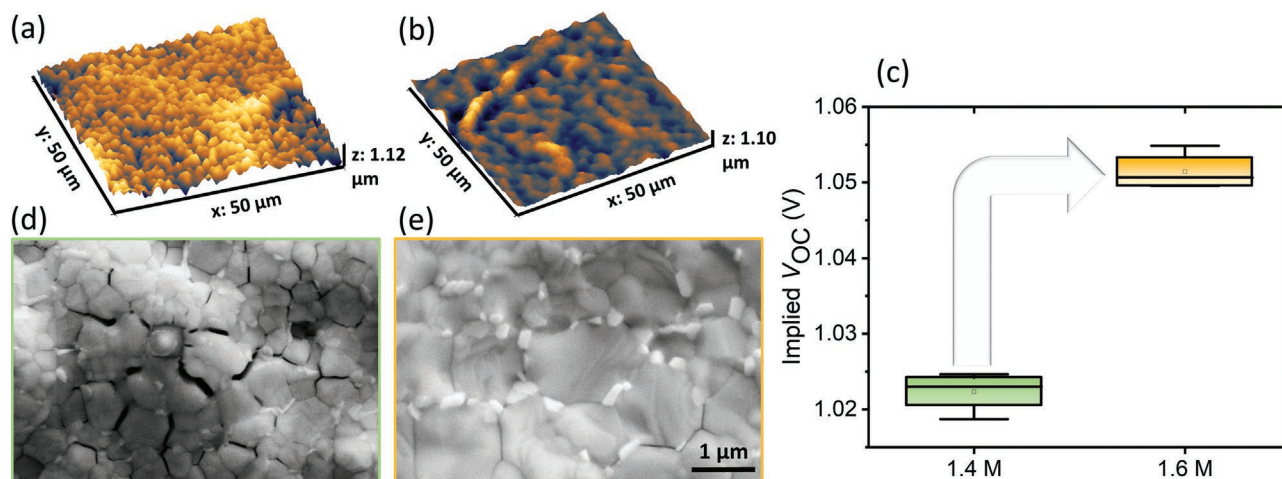

Figure 4. a,b) 3D AFM representation of the half-stack ITO/NiO_x/2PACz/perovskite/C_{60} over textured Si substrate deposited using 1.4 and 1.6 M perovskite precursor solution respectively. c) Implied V_{OC} comparison of the two cases. d,e) Top view SEM images for the two corresponding perovskite thin films.

is reduced to ≈115 nm. As a reference, the corresponding thicknesses of the perovskite thin films deposited over a planar substrate using 1.4 and 1.6 м are ≈720 and ≈960 nm, respectively. As expected, PSCs with 1.4 м precursor solution therefore exhibit an evident reduction in the shunt resistance as compared the fully covered PSCs (see Figure S12, Supporting Information).

In addition to the high surface roughness, we note that the perovskite films deposited using the 1.4 м solution tend to form surface cracks around the pyramidal tips as evidenced by the top view SEM images in Figure 4d and Figure S13 (Supporting Information). Surface cracks along with high surface roughness potentially results in a poor perovskite/ETL interface and consequently a high non-radiative recombination rate.[123] Indeed, as indicated by the PLQY measurements of the half-stack ITO/NiO_x/2PACz/perovskite/C_{60} shown in Figure 4c, the voltage losses of the fully covered surface that corresponds to the 1.6 м solution is much lower, with an implied V_{OC} of 1.051 V compared to 1.022 V in case of using the lower concentration solution.

2.5. Solvent Engineering Impact on the Morphology and Voltage Losses

As discussed in the previous sections, assuring full surface coverage by using a perovskite precursor solution with relatively high concentration together with optimized processing parameters prevents detrimental shunting paths and leads to enhancement in V_{OC}.[3,27,35,38,80] However, the pyramidal tips that reach out the surface in case of low perovskite precursor solution concentration are not the only reason for the high surface roughness. Although the thorough surface coverage condition is fulfilled when using high concentration solution, we note that the perovskite films still suffer from high voltage losses at the perovskite/ETL interface.

By further microstructural investigation using AFM and SEM, we find that the perovskite film deposited using the high concentration 1.6 м precursor solution with the standard 1:4 DMSO:N,N-dimethylformamide (DMF) (20% DMSO) volume ratio exhibits high density, randomly distributed surface wrinkles with considerable height (see **Figure 5**a,d; Figure S14, Supporting Information). These surface wrinkles with their considerable height and width can show a strong effect on the surface roughness of the perovskite thin film, potentially resulting in a poor perovskite/ETL interface.[112,123–132] Hence, controlling the surface wrinkles formation in perovskite films processed over micrometer-sized textures is crucial in minimizing the V_{OC} losses.

The 3D representation of a 50 × 50 µm² AFM scan in Figure 5a displays a representative surface wrinkle with an average height of ≈1.5 µm and average width of ≈4.8 µm as
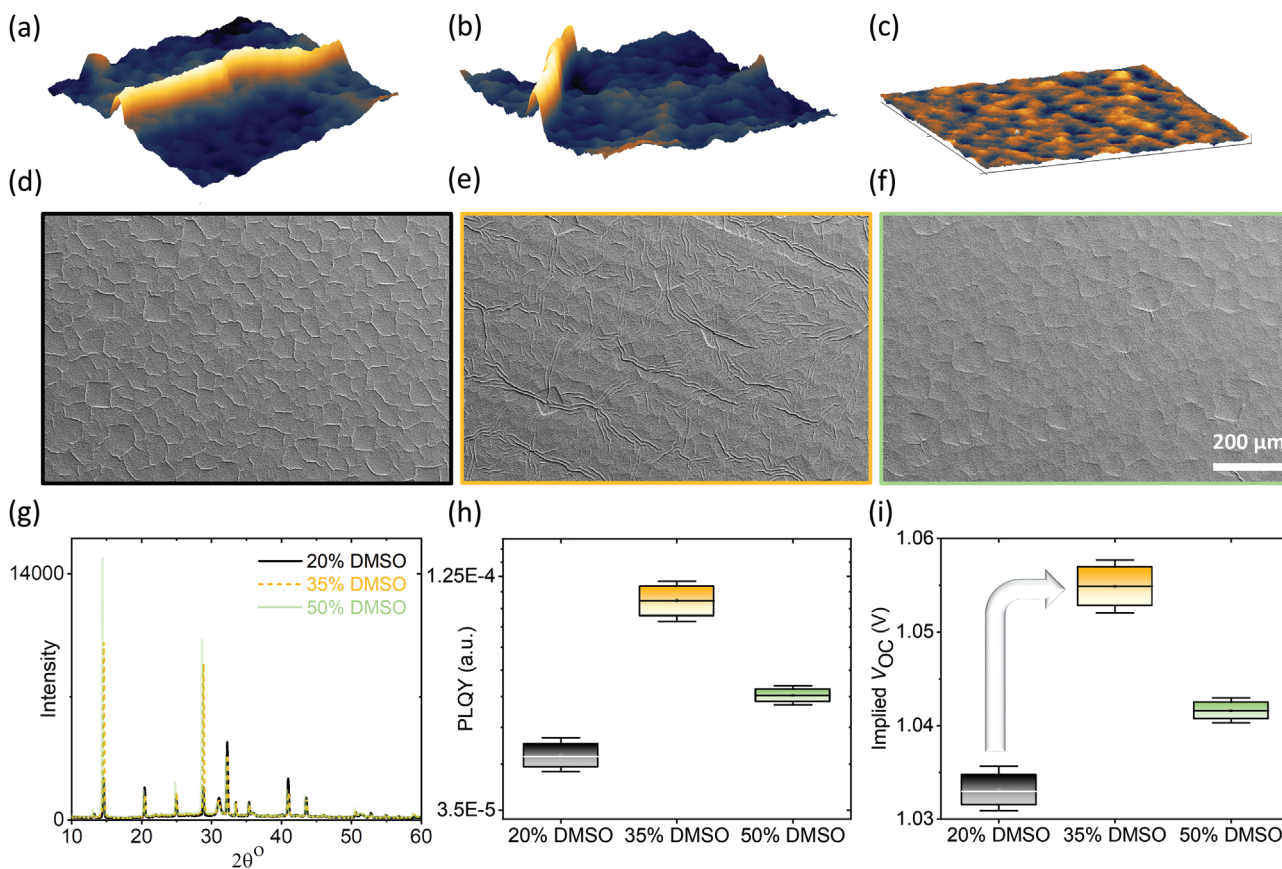

Figure 5. a–c) 3D representation of AFM measurements for perovskite films processed over the textured half-stack ITO/NiO_x/2PACz/perovskite using 20%, 35%, and 50 % DMSO ratio respectively. d–f) Corresponding top view SEM images. g) Corresponding XRD measurements. h,i) PLQY intensity and implied V_{OC} comparison after introducing C_{60} onto the half-stack.

**ADVANCED
SCIENCE NEWS**

www.advancedsciencenews.com

**ADVANCED
FUNCTIONAL
MATERIALS**

www.afm-journal.de

shown in Figure S15 (Supporting Information). Within the scanned area, this wrinkle increases the RMS roughness (≈500 nm). Wrinkles in perovskite thin films occur when the substrate constrains the film from expansion, consequently, the in-plane compressive stress that occurs during the intermediate phase of film formation results in energy release in the form of wrinkles.[125] With the anti-solvent quenching method, volume changes between the film and the underlying substrate results in residual stress in the perovskite film.[126] Perovskite composition,[127–129,132] processing parameters,[112,132] solvent type/ratio, and last but not least the substrate type, morphology, and temperature,[124,129,130] have strong impact on surface wrinkles formation. Excessive formation of wrinkles can lead to micro-cracks, which might act as non-radiative recombination centers.[123,130] Furthermore, it has been found that strain caused by the thermal expansion mismatch between the perovskite material and substrate can accelerate the perovskite decomposition.[124] Reducing the strain gradient of the perovskite film leads to improvement in hole transport and extraction and enhances V_{OC} in planar PSCs.[131] The substrate dependence of residual stress is expected to be more complex when depositing the film over a textured surface, indicating that controlling the film surface roughness becomes crucial to minimize V_{OC} losses.

To study the effect of reducing the strain-related surface wrinkles on the non-radiative recombination at the perovskite/ETL interface, we optimized the solvents ratio to control the wrinkles formation and consequently, the surface roughness of the film as well as its crystallinity.

Increasing the DMSO percentage in the perovskite precursor solution from 20% to 35% and 50% tends to have an impact on density, height, and width of wrinkles as depicted in top view SEM images in Figure 5 and Figure S14 (Supporting Information). Although wrinkles are still present in the 35% DMSO film with a comparable height to that of the reference (20% DMSO), wrinkle width is at least 25% smaller. Furthermore, the number of wrinkles per unit area is strongly reduced. As a result, RMS roughness decreases from ≈500 nm in the reference to ≈335 nm when 35% DMSO is used. Increasing the DMSO ratio further to 50% results in a way lower RMS roughness of ≈93 nm and wrinkles are barely noticeable. Furthermore, the DMSO ratio plays a key role in the crystallization dynamics.[125,133–136] We observed improved crystallinity for films with higher DMSO ratio as indicated by the (100) and (200) peak intensities in the XRD measurements (Figure 5g). We note we observe small shifts in the XRD peak positions, which might be related to micro-strain.[126,131,137,138]

Non-radiative recombination at the perovskite/C_{60} interface is significantly reduced when the DMSO ratio is 35% because of reduced wrinkles density and the consequent reduced surface roughness compared to the reference with the standard 20% ratio. The implied V_{OC} is 1.059 V in case of 35% DMSO compared to 1.038 V for the standard 20% (Figure 5i). Although further increasing the DMSO ratio to 50% considerably reduced surface roughness, implied V_{OC} was found to be lower for this higher ratio (1.047 V) than the 35% DMSO case but remained higher than the 20% DMSO reference, in full agreement with the external V_{OC} data in Figure S16 (Supporting Information). It has been shown that a controlled wrinkled morphology could

potentially lead to increased V_{OC} as the hill sites with higher amplitude of wrinkles exhibit less defects.[129] We hypothesize it could be one of the potential reasons that the V_{OC} doesn't increase any further by eliminating the surface wrinkles (as it happens when using 50% DMSO).

2.6. Surface Passivation and Voltage Losses

Choosing a proper HTL and optimizing the excess PbI_2 minimizes the losses at the HTL/perovskite interface and the bulk itself, leaving the perovskite/ETL to be the limiting interface. Taking into account the very significant voltage losses at the perovskite/ETL interface in the p–i–n planar PSCs,[44,49,139,140] these losses are expected to be even higher in case of processing onto micrometer-sized textured substrates due to the expected increase in surface roughness of the perovskite film.

Having developed high-quality perovskite film with good surface coverage, morphology, and optoelectronic properties over the micrometer-sized texture, surface passivation of the perovskite/ETL interface is discussed in the following. We show that both solution-processed and thermally evaporated surface passivation interlayer can reduce drastically the non-radiative recombination at the perovskite/C_{60} interface.

Given the known high defect density at the perovskite/C_{60} interface,[27,38,44,49] PLQY of the reference stack ITO/NiO$_x$/2PACz/perovskite/C_{60} processed over a micrometer-sized texture is low (0.0061%), which corresponds to an implied V_{OC} of only 1.045 V (see **Figure 6**). However, 1 nm of thermally evaporated lithium fluoride (LiF) interlayer in-between the perovskite thin film and the C_{60} layer, already increases average PLQY to 0.018% with a corresponding implied V_{OC} of 1.073 V. This is an improvement in implied V_{OC} of ≈30 mV, which is in good agreement with previous reports.[12,41,141,142] However while LiF is a simple and widely used passivation interlayer, significantly better interlayers have been suggested in literature for the perovskite/ETL interface. For example, we demonstrated in our previous work that the long-chain alkylammonium salt phenethylammonium chloride (PEACl) has a remarkable contribution in reducing the losses at the perovskite/C_{60} interface in planar PSCs.[49] Here, we investigate the role that PEACl plays in passivating the same interface when perovskite films are deposited over micrometer-sized texture, by spin-coating two different concentrations (namely 1 and 2 mg mL^{-1}). The lower concentration of PEACl contributed significantly in enhancing implied V_{OC} (≈40 mV higher than the reference), and is already outperforming the LiF (external V_{OC} data of the full device stack match with the implied V_{OC} data as shown in Figure S17, Supporting Information). The higher concentration has shown an impressive enhancement in PLQY (almost one order of magnitude higher than the reference) and a corresponding implied V_{OC} of 1.106 V. Higher concentrations of PEACl are expected to boost the implied V_{OC} further, but it might cause short-circuit current density and FF losses as reported in our previous work.[49] We also performed intensity-dependent measurements of the stacks with C_{60} to analyze n_{id} of the different stacks (see Figure S18, Supporting Information). We find that both concentrations of PEACl yield n_{id} of ≈1.46, which is slightly lower as compared to the reference and LiF that both show n_{id} of ≈1.50.
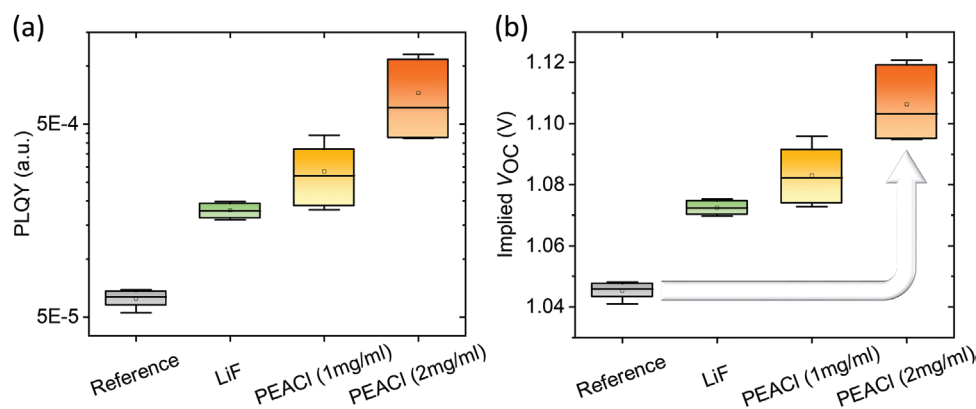
Figure 6. a,b) PLQY and implied V_{OC} comparison between different surface passivation layers deposited in between the perovskite and C_{60} in the half-stack ITO/NiO$_x$/2PACz/perovskite/C$_{60}$ processed over micrometer-sized textured Si substrates.

While this reduction is a bit smaller compared to our previous work,[49] it is in line with a reduction in trap-assisted Shockley-Read Hall recombination at the perovskite/C$_{60}$ interface. Similarly, to PEACl and LiF, alternative promising options for surface passivation have emerged recently in literature. De Wolf and co-workers have shown that thermally evaporating 1 nm of MgF$_x$ as an interlayer in-between the perovskite thin film and the C$_{60}$ layer, mitigates non-radiative recombination. Furthermore, the long-term stability that these PSCs exhibit is quite remarkable.[27] Also, a double layer of LiF and guanidinium bromide have shown V_{OC} enhancement in wide band gap p–i–n PSCs.[119]

3. Conclusion

In this study, we quantify voltage losses in solution-processed perovskite thin films over micrometer-sized textured Si wafers using PLQY. With various characterization tools, we identify potential reasons behind these losses and offer ideas to tackle them. Due to the large surface area that a textured substrate exhibits, a conformal sputtered HTL in combination with a high-performance solution-processed SAM can lead to implied V_{OC} gains as high as 50 mV. Choosing optimum deposition parameters eliminates formation of voids in the pyramid valleys, both enhancing charge extraction (i.e., ≈8.5% higher FF) and reducing non-radiative recombination (i.e., 10–15 mV higher V_{OC}). Assuring full surface coverage by choosing the optimum perovskite solution concentration prevents micro-crack formation around the pyramidal tips and consequently attributes to average gains of 30 mV. By controlling the surface wrinkles formation via solvent engineering strategy, one can gain up to 20 mV. By optimizing excess PbI$_2$, we gain an average of 55 mV higher than perovskite films processed using a stoichiometric solution. In addition, with different surface passivation methods, we can boost the gains further by 30–60 mV. To the best of our knowledge, this is the first study that in detail investigates the various voltage losses in perovskite thin films processed over textured surfaces. This work initiates and strengthens the understanding of this timely research topic.

4. Experimental Section

Textured Si Wafers: To remove the saw damage, residuals, and contamination; a pre-cleaning step was done first. Afterward, alkaline KOH solution with surface activating additives was used to anisotropic etch *p*-type, monocrystalline, <100> silicon wafers. Post cleaning was done using HF/HCL. More details could be found in ref. [143]

Wafer Type: A p-type wafer was recommended to use as a substrate if an inverted stack was going to be processed onto it. A buffer layer of SiO$_x$ or Al$_2$O$_3$ over the textured substrate was beneficial in case of patterned ITO is going to be used. A comparison between PSCs employing *n* and *p*-type Si wafers was shown in Figure S19 (Supporting Information).

Device Fabrication: *Back Contact*: 135 nm of patterned indium tin oxide (ITO) as a back electrode was sputtered using Kurt J. Lesker PVD-75 thin film deposition system. The substrates were heated up to 300 °C for 75 min in the vacuum chamber before deposition and this temperature was maintained during the whole deposition process, the deposition parameters can be found in ref. [80] The average sheet resistance of the ITO films was ≈14 Ω cm^{-2}.

Hole Transport Layer (HTL): The substrates with TCO were heated up to 150 °C for 25 min in the vacuum chamber, then 15 nm NiO$_x$ film was sputtered from a NiO$_x$ target using 100 W power with pure Ar at 1 mTorr. The solution processed 2PACz was deposited via spin-coating as detailed in ref. [65]

Perovskite: 1.6 M (or 1.4 M) of the double-cation Cs$_{0.17}$FA$_{0.83}$PbI$_{2.75}$Br$_{0.25}$ precursor solution was prepared by mixing lead iodide (PbI$_2$, TCI) and lead bromide (PbBr$_2$, TCI) and dissolve them together in 80:20 (65:35 or 50:50) N,N-Dimethylformamide (DMF, Sigma–Aldrich):dimethyl sulfoxide (DMSO, Sigma–Aldrich). The solution was heated up for 30 min at 130 °C and left to cool down for 10 min. Afterward, the mixed solution was transferred to the cesium iodide (CsI, Alfa Aesar) and formamidinium iodide (FAI, Great Cell Solar) and vigorously agitated until all the powders were dissolved. Depending on each case, 0%, 10%, 15%, or 20% excess PbI$_2$ was employed in the precursor solution. The spin-coating program referred to as early quenching was a two-step program: 200 rpm with 300 rpm s^{-1} for 2 s followed by 2000 rpm with 2000 rpm s^{-1} for 30 s. A solvent quenching step of (150 µL) of Ethyl acetate anhydrous, 99.8% (C$_4$H$_8$O$_2$, Sigma–Aldrich) was dispensed 15–18 s before the end of the 2nd step. For late quenching, a two-step program: 200 rpm with 300 rpm s^{-1} for 2 s followed by 2000 rpm with 2000 rpm s^{-1} for 60 s. (150 µL) of anhydrous Ethyl acetate was dispensed 5 s before the end of the 2nd step. All samples were annealed for 30 min at 100 °C. The triple-cation Cs$_{0.05}$MA$_{0.22}$FA$_{0.73}$Pb(I$_{0.77}$Br$_{0.23}$)$_3$ was prepared as described in ref. [74]

Surface Passivation: 1 nm of LiF was thermally evaporated as stated in previous work.[144] Solution-processed surface passivation was prepared by dissolving (1–2 mg) 2-phenylethylammonium chloride (PEACl:Sigma-Aldrich) in (1 mL) 2-Propanol (IPA, Sigma–Aldrich) and dynamically

spin-coated on top of the perovskite film using 1 step program with 5000 rpm and 2000 rpm s^{-1}, the film was annealed for 5 min at 100 °C. More details can be found in our previous work.[49]

Electron Transport Layer (ETL): 25 nm thick fullerene (C$_{60}$, Alfa Aesar) was thermally evaporated and deposited using an OPTIvap evaporation system at a pressure of 5×10^{-7} mbar with a deposition rate of 0.4° A s^{-1}. A 35 nm SnO$_x$ film was deposited afterward over 300 cycles using ALD. The following settings were used: a 1.6 s TDMASn pulse with 12 s of purging then a 0.1 s water pulse with 16 s of purging. A boosting system, increasing line flow to 500 sccm immediately prior to pulsing, was utilized instead of the conventional bubbler due to system layout.

Front Contact: 165 nm of IZO was deposited using a Kurt J. Lesker PVD-75 thin film deposition system. The deposition parameters were: 100 W of RF power over 4 inch^2 and a deposition time of 2550 s at 1 mTorr pressure with 1% oxygen to argon ratio. A 100 nm silver contact grid was thermally evaporated at 1° A s^{-1} afterward.

Characterization Methods: *Glow discharge optical emission spectroscopy (GDOES)*: Depth profiles for the compositional elements in the stack were recorded using a Horiba Scientific GD-Profiler 2 glow discharge optical emission spectrometer. The measurements were done using RF-mode at a power of 26 W and 5 mbar of argon pressure. The inspection spot was ≈4 mm in diameter.

Time-of-flight secondary ion mass spectrometry (ToF-SIMS): A time-of-flight secondary ion mass spectrometer from IONTOF was used to analyze the potential reactions at the HTL/perovskite interface by measuring the depth profiling. A 30 KeV bismuth ion (Bi$^+$) was used as analyzing beam and probed over an area of 50×50 μm^2. For sputtering, a 2 KeV cesium ion (Cs$^+$) beam was used to form cesium clusters with the electropositive and electronegative elements. The rasterized area was 300×300 μm^2. More details can be found in previous work.[145]

X-ray diffraction (XRD): A Bruker D2Phaser system was used with Cu-K$_\alpha$ radiation in Bragg–Brenton configuration to identify the crystal structure of the perovskite films.

Photoluminescence quantum yield (PLQY): PLQY measurements were carried out inside an integrating sphere (LabSphere, 15 cm diameter) flushed with nitrogen (relative humidity <5%). A green laser (LD-515-10MG from Roithner Lasertechnik) was directed into the sphere via a small entrance port. An optical fiber was used to collect the emission from the exit port of the sphere and guide it to the spectrometers (QEPro from Ocean Optics). The spectral response was calibrated using a calibration lamp (HL-3plus-INT-Cal from Ocean Optics) and raw measured spectra were recalculated to give power spectra using the integration time. The PLQY was determined using the method described by de Mello et al.[146] The samples were placed at an angle of 15° with respect to the laser beam to avoid specular reflectance. The implied V_{OC} was determined from the (intensity-dependent) PLQY measurements as described by Stolterfoht et al.[42] and Kirchartz et al.[147] $J_{0,rad}$ was determined using the EQE obtained from the following semi-transparent device stack: textured Si/patterned ITO/NiO$_x$/2PACz/perovskite/C$_{60}$/SnO$_x$/IZO/Ag grid (see Figure S20, Supporting Information). Since there was no obvious change in the EQE spectrum close to the bandgap for the various processing conditions studied in this work, the same $J_{0,rad}$ was used for the calculations of all implied V_{OC}'s.

Scanning electron microscopy (SEM): Top-view and cross-sectional, high-resolution SEM images, were obtained using Zeiss LEO1530 VP model with 10–20 μm aperture size and an in-lens detector. The images were captured using acceleration voltage of 5–10 kV.

Current density–voltage (J–V) measurements: A class AAA Newport Oriel Sol3A solar simulator (xenon lamp) was used. Before performing the measurements, the solar simulator was calibrated using a certified Si photodiode equipped with a KG5 band pass filter. More details can be found in our previous work.[148]

Supporting Information

Supporting Information is available from the Wiley Online Library or from the author.

Conflict of Interest

The authors declare no conflict of interest.

Author Contributions

U.W.P. supervised the whole project. A.F. conceived the idea of this study with support of P.F. and U.W.P. A.F. planned the experiments, fabricated the perovskite films, optimized the fabrication-related procedures, and performed the AFM, SEM, J-V, EQE, XRD, and EDX measurements and the corresponding data analysis. P.F. performed the PLQY and the corresponding data analysis. W.H. performed the ToF-SIMS measurements and D.B. performed the GDOES, the data were analyzed by W.H., D.B., and A.F. The ALD was done by T.F. and H.H. The cross-sectional SEM images were taken by A.Q. M.A.R helped in writing and correcting the manuscript. B.W., P.N., and T.D. fabricated the textured Si wafers. All authors have contributed in correcting and enhancing the quality of the discussion in the paper.

Data Availability Statement

The data that support the findings of this study are available in the supplementary material of this article.

[1] J. P. Mailoa, C. D. Bailie, E. C. Johlin, E. T. Hoke, A. J. Akey, W. H. Nguyen, M. D. McGehee, T. Buonassisi, *Appl. Phys. Lett.* **2015**, *106*, 121105.

[2] F. E. Subhan, A. D. A. D. Khan, A. D. A. D. Khan, N. Ullah, M. Imran, M. Noman, *RSC Adv.* **2020**, *10*, 26631.

[3] M. De Bastiani, A. J. Mirabelli, Y. Hou, F. Gota, E. Aydin, T. G. Allen, J. Troughton, A. S. Subbiah, F. H. Isikgor, J. Liu, L. Xu, B. Chen, E. Van Kerschaver, D. Baran, B. Fraboni, M. F. Salvador, U. W. Paetzold, E. H. Sargent, S. De Wolf, *Nat. Energy* **2021**, *6*, 167.

[4] E. Köhnen, M. Jošt, A. B. Morales-Vilches, P. Tockhorn, A. Al-Ashouri, B. Macco, L. Kegelmann, L. Korte, B. Rech,

R. Schlatmann, B. Stannowski, S. Albrecht, *Sustainable Energy Fuels* **2019**, *3*, 1995.

[5] J. Xu, C. C. Boyd, Z. J. Yu, A. F. Palmstrom, D. J. Witter, B. W. Larson, R. M. France, J. Werner, S. P. Harvey, E. J. Wolf, W. Weigand, S. Manzoor, M. F. A. M. Van Hest, J. J. Berry, J. M. Luther, Z. C. Holman, M. D. McGehee, *Science* **2020**, *367*, 1097.

[6] G. Nogay, F. Sahli, J. Werner, R. Monnard, M. Boccard, M. Despeisse, F. J. Haug, Q. Jeangros, A. Ingenito, C. Ballif, *ACS Energy Lett.* **2019**, *4*, 844.

[7] M. Roß, S. Severin, M. Björn Stutz, P. Wagner, H. Köbler, M. Favin-Lévêque, A. Al-Ashouri, P. Korb, P. Tockhorn, A. Abate, B. Stannowski, B. Rech, S. Albrecht, *Advanced Energy Materials* **2021**, *11*, 2101460.

[8] M. Jošt, E. Köhnen, A. B. Morales-Vilches, B. Lipovšek, K. Jäger, B. Macco, A. Al-Ashouri, J. Krč, L. Korte, B. Rech, R. Schlatmann, M. Topič, B. Stannowski, S. Albrecht, *Energy Environ. Sci.* **2018**, *11*, 3511.

[9] J. Y. Hyun, K. M. Yeom, S.-W. Lee, S. Bae, D. Choi, H. Song, D. Kang, J.-K. Hwang, W. Lee, S. Lee, Y. Kang, H.-S. Lee, J. H. Noh, D. Kim, *ACS Appl. Energy Mater.* **2022**, *10*, 44.

[10] J. Roger, L. K. Schorn, M. Heydarian, A. Farag, T. Feeney, D. Baumann, H. Hu, F. Laufer, W. Duan, K. Ding, A. Lambertz, P. Fassl, M. Worgull, U. W. Paetzold, *Adv. Energy Mater.* **2022**, *12*, 2200961.

[11] F. Gota, R. Schmager, A. Farag, U. W. Paetzold, *Opt. Express* **2022**, *30*, 14172.

[12] A. Al-Ashouri, E. Köhnen, B. Li, A. Magomedov, H. Hempel, P. Caprioglio, J. A. Márquez, A. B. M. Vilches, E. Kasparavicius, J. A. Smith, N. Phung, D. Menzel, M. Grischek, L. Kegelmann, D. Skroblin, C. Gollwitzer, T. Malinauskas, M. Jošt, G. Matič, B. Rech, R. Schlatmann, M. Topič, L. Korte, A. Abate, B. Stannowski, D. Neher, M. Stolterfoht, T. Unold, V. Getautis, S. Albrecht, *Science* **2020**, *370*, 1300.

[13] H. Shen, D. Walter, Y. Wu, K. C. Fong, D. A. Jacobs, T. Duong, J. Peng, K. Weber, T. P. White, K. R. Catchpole, *Adv. Energy Mater.* **2020**, *10*, 1902840.

[14] Y. Hu, L. Song, Y. Chen, W. Huang, *Sol. RRL* **2019**, *3*, 1970116.

[15] W. Qarony, M. I. Hossain, V. Jovanov, A. Salleo, D. Knipp, Y. H. Tsang, *ACS Appl. Mater. Interfaces* **2020**, *12*, 15080.

[16] B. Chen, Z. Yu, K. Liu, X. Zheng, J. Liu, J. Shi, D. Spronk, P. N. Rudd, Z. Holman, J. Huang, *Joule* **2019**, *3*, 177.

[17] E. Köhnen, P. Wagner, F. Lang, A. Cruz, B. Li, M. Roß, M. Jošt, A. B. Morales-Vilches, M. Topič, M. Stolterfoht, D. Neher, L. Korte, B. Rech, R. Schlatmann, B. Stannowski, S. Albrecht, *Sol. RRL* **2021**, *5*, 2100244.

[18] K. A. Bush, A. F. Palmstrom, Z. J. Yu, M. Boccard, R. Cheacharoen, J. P. Mailoa, D. P. McMeekin, R. L. Z. Hoye, C. D. Bailie, T. Leijtens, I. M. Peters, M. C. Minichetti, N. Rolston, R. Prasanna, S. Sofia, D. Harwood, W. Ma, F. Moghadam, H. J. Snaith, T. Buonassisi, Z. C. Holman, S. F. Bent, M. D. McGehee, *Nat. Energy* **2017**, *2*, 17009.

[19] S. M. Iftiquar, J. Jung, J. Yi, J. Liu, H. Wen, L. Shen, A. De Vos, *J Phys D Appl Phys* **1980**, *13*, 839.

[20] S. Rühle, *Sol. Energy* **2016**, *130*, 139.

[21] Best Research-Cell Efficiency Chart | Photovoltaic Research | NREL.

[22] F. Gota, M. Langenhorst, R. Schmager, J. Lehr, U. W. Paetzold, *Joule* **2020**, *4*, 2387.

[23] P. Tockhorn, P. Wagner, L. Kegelmann, J. C. Stang, M. Mews, S. Albrecht, L. Korte, *ACS Appl. Energy Mater.* **2020**, *3*, 1381.

[24] I. J. Park, J. H. Park, S. G. Ji, M. A. Park, J. H. Jang, J. Y. Kim, *Joule* **2019**, *3*, 807.

[25] H. Kanda, V. D. Mihailetchi, M.-E. Gueunier-Farret, J.-P. Kleider, Z. Djebbour, J. Alvarez, B. Philippe, O. Isabella, M. R. Vogt, R. Santbergen, P. Schulz, F. Peter, M. K. Nazeeruddin, J. P. Connolly, *Interdiscip. Mater.* **2022**, *1*, 148.

[26] E. L. Warren, W. E. Mcmahon, M. Rienäcker, K. T. Vansant, R. C. Whitehead, R. Peibst, A. C. Tamboli, *ACS Energy Lett.* **2020**, *5*, 1233.

[27] J. Liu, M. De Bastiani, E. Aydin, G. T. Harrison, Y. Gao, R. R. Pradhan, M. K. Eswaran, M. Mandal, W. Yan, A. Seitkhan, M. Babics, A. S. Subbiah, E. Ugur, F. Xu, L. Xu, M. Wang, A. ur Rehman, A. Razzaq, J. Kang, R. Azmi, A. A. Said, F. H. Isikgor, T. G. Allen, D. Andrienko, U. Schwingenschlögl, F. Laquai, S. De Wolf, *Science* **2022**, *8910*, 2003.

[28] A. S. Subbiah, F. H. Isikgor, C. T. Howells, M. De Bastiani, J. Liu, E. Aydin, F. Furlan, T. G. Allen, F. Xu, S. Zhumagali, S. Hoogland, E. H. Sargent, I. McCulloch, S. De Wolf, *ACS Energy Lett.* **2020**, *5*, 3034.

[29] F. H. Isikgor, F. Furlan, J. Liu, E. Ugur, M. K. Eswaran, A. S. Subbiah, E. Yengel, M. De Bastiani, G. T. Harrison, S. Zhumagali, C. T. Howells, E. Aydin, M. Wang, N. Gasparini, T. G. Allen, A. ur Rehman, E. Van Kerschaver, D. Baran, I. McCulloch, T. D. Anthopoulos, U. Schwingenschlögl, F. Laquai, S. De Wolf, *Joule* **2021**, *5*, 1566.

[30] L. Gil-Escrig, M. Roß, J. Sutter, A. Al-Ashouri, C. Becker, S. Albrecht, *Sol. RRL* **2021**, *5*, 2000553.

[31] K. Hamada, K. Yonezawa, K. Yamamoto, T. Taima, S. Hayase, N. Ooyagi, Y. Yamamoto, K. Ohdaira, *Jpn. J. Appl. Phys.* **2019**, *58*, SBBF06.

[32] F. Sahli, J. Werner, B. A. Kamino, M. Bräuninger, R. Monnard, B. Paviet-Salomon, L. Barraud, L. Ding, J. J. Diaz Leon, D. Sacchetto, G. Cattaneo, M. Despeisse, M. Boccard, S. Nicolay, Q. Jeangros, B. Niesen, C. Ballif, *Nat. Mater.* **2018**, *17*, 820.

[33] S.-W. Lee, S. Bae, J.-K. Hwang, W. Lee, S. Lee, J. Y. Hyun, K. Cho, S. Kim, F. D. Heinz, S. Bin Choi, D. Choi, D. Kang, J. Yang, S. Jeong, S. J. Park, M. C. Schubert, S. Glunz, W. M. Kim, Y. Kang, H.-S. Lee, D. Kim, *Commun Chem* **2020**, *3*, 37.

[34] L. Mao, T. Yang, H. Zhang, J. Shi, Y. Hu, P. Zeng, F. Li, J. Gong, X. Fang, Y. Sun, X. Liu, J. Du, A. Han, L. Zhang, W. Liu, F. Meng, X. Cui, Z. Liu, M. Liu, *Adv. Mater.* **2022**, *7*, 2206193.

[35] B. Chen, Z. J. Yu, S. Manzoor, S. Wang, W. Weigand, Z. Yu, G. Yang, Z. Ni, X. Dai, Z. C. Holman, J. Huang, *Joule* **2020**, *4*, 850.

[36] E. Aydin, J. Liu, E. Ugur, R. Azmi, G. T. Harrison, Y. Hou, B. Chen, S. Zhumagali, M. De Bastiani, M. Wang, W. Raja, T. G. Allen, A. ur Rehman, A. S. Subbiah, M. Babics, A. Babayigit, F. H. Isikgor, K. Wang, E. Van Kerschaver, L. Tsetseris, E. H. Sargent, F. Laquai, S. De Wolf, *Energy Environ. Sci.* **2021**, *14*, 4377.

[37] J. Wang, C. Gao, X. Wang, Y. Wang, Z. Cheng, H. Liu, W. Shen, *Energy Technol.* **2021**, *9*, 2000778.

[38] Y. Hou, E. Aydin, M. De Bastiani, C. Xiao, F. H. Isikgor, D. J. Xue, B. Chen, H. Chen, B. Bahrami, A. H. Chowdhury, A. Johnston, S. W. Baek, Z. Huang, M. Wei, Y. Dong, J. Troughton, R. Jalmood, A. J. Mirabelli, T. G. Allen, E. Van Kerschaver, M. I. Saidaminov, D. Baran, Q. Qiao, K. Zhu, S. De Wolf, E. H. Sargent, *Science* **2020**, *367*, 1135.

[39] X. Zheng, J. Liu, T. Liu, E. Aydin, M. Chen, W. Yan, M. De Bastiani, T. G. Allen, S. Yuan, A. R. Kirmani, K. N. Baustert, M. F. Salvador, B. Turedi, A. Y. Alsalloum, K. Almasabi, K. Kotsovos, I. Gereige, L.-S. Liao, J. M. Luther, K. R. Graham, O. F. Mohammed, S. De Wolf, O. M. Bakr, *ACS Energy Lett.* **2022**, *2022*, 1987.

[40] K. Sveinbjörnsson, B. Li, S. Mariotti, E. Jarzembowski, L. Kegelmann, A. Wirtz, F. Frühauf, A. Weihrauch, R. Niemann, L. Korte, F. Fertig, J. W. Müller, S. Albrecht, *ACS Energy Lett.* **2022**, *7*, 2654.

[41] M. Stolterfoht, P. Caprioglio, C. M. Wolff, J. A. Márquez, J. Nordmann, S. Zhang, D. Rothhardt, U. Hörmann, Y. Amir, A. Redinger, L. Kegelmann, F. Zu, S. Albrecht, N. Koch, T. Kirchartz, M. Saliba, T. Unold, D. Neher, *Energy Environ. Sci.* **2019**, *12*, 2778.

**ADVANCED
SCIENCE NEWS**

www.advancedsciencenews.com

**ADVANCED
FUNCTIONAL
MATERIALS**

www.afm-journal.de

[42] M. Stolterfoht, M. Grischek, P. Caprioglio, C. M. Wolff, E. Gutierrez-Partida, F. Peña-Camargo, D. Rothhardt, S. Zhang, M. Raoufi, J. Wolansky, M. Abdi-Jalebi, S. D. Stranks, S. Albrecht, T. Kirchartz, D. Neher, *Adv. Mater.* **2020**, *32*, 2000080.

[43] C. M. Wolff, S. A. Bourelle, L. Q. Phuong, J. Kurpiers, S. Feldmann, P. Caprioglio, J. Antonio Marquez, J. Wolansky, T. Unold, M. Stolterfoht, S. Shoaee, F. Deschler, D. Neher, C. M. Wolff, J. Kurpiers, P. Caprioglio, J. Wolansky, M. Stolterfoht, D. Neher, S. A. Bourelle, S. Feldmann, F. Deschler, L. Q. Phuong, J. Kurpiers, S. Shoaee, J. A. Marquez, T. Unold, *Adv. Energy Mater.* **2021**, *11*, 2101823.

[44] J. Warby, F. Zu, S. Zeiske, E. Gutierrez-Partida, L. Frohloff, S. Kahmann, K. Frohna, E. Mosconi, E. Radicchi, F. Lang, S. Shah, F. Peña-Camargo, H. Hempel, T. Unold, N. Koch, A. Armin, F. De Angelis, S. D. Stranks, D. Neher, M. Stolterfoht, *Adv. Energy Mater.* **2022**, *12*, 2103567.

[45] R. Islam, G. Chen, P. Ramesh, J. Suh, N. Fuchigami, D. Lee, K. A. Littau, K. Weiner, R. T. Collins, K. C. Saraswat, *ACS Appl. Mater. Interfaces* **2017**, *9*, 17201.

[46] A. K. M. Hasan, A. K. M. Hasan, I. Raifuku, N. Amin, N. Amin, Y. Ishikawa, D. K. Sarkar, K. Sobayel, M. R. Karim, A. Ul-Hamid, H. Abdullah, M. Shahiduzzaman, Y. Uraoka, K. Sopian, M. Akhtaruzzaman, M. Akhtaruzzaman, M. Akhtaruzzaman, *Opt. Mater. Express* **2020**, *10*, 1801.

[47] T. Abzieher, S. Moghadamzadeh, F. Schackmar, H. Eggers, F. Sutterlüti, A. Farooq, D. Kojda, K. Habicht, R. Schmager, A. Mertens, R. Azmi, L. Klohr, J. A. Schwenzer, M. Hetterich, U. Lemmer, B. S. Richards, M. Powalla, U. W. Paetzold, *Adv. Energy Mater.* **2019**, *9*, 1802995.

[48] D. Di Girolamo, F. Di Giacomo, F. Matteocci, A. G. Marrani, D. Dini, A. Abate, D. Di Girolamo, *Chem. Sci.* **2020**, *11*, 7746.

[49] S. Gharibzadeh, P. Fassl, I. M. Hossain, P. Rohrbeck, M. Frericks, M. Schmidt, T. Duong, M. R. Khan, T. Abzieher, B. A. Nejand, F. Schackmar, O. Almora, T. Feeney, R. Singh, D. Fuchs, U. Lemmer, J. P. Hofmann, S. A. L. Weber, U. W. Paetzold, *Energy Environ. Sci.* **2021**, *14*, 5875.

[50] H.-S. Kim, J.-Y. Seo, H. Xie, M. Lira-Cantu, S. M. Zakeeruddin, M. Grätzel, A. Hagfeldt, *ACS Omega* **2017**, *2*, 9074.

[51] M. Michalska, M. A. Surmiak, F. Maasoumi, D. C. Senevirathna, P. Chantler, H. Li, B. Li, T. Zhang, X. Lin, H. Deng, N. Chandrasekaran, T. A. N. Peiris, K. J. Rietwyk, A. S. R. Chesman, T. Alan, D. Vak, U. Bach, J. J. Jasieniak, *Sol. RRL* **2021**, *5*, 2100342.

[52] I. J. Park, G. Kang, M. A. Park, J. Y. J. S. Kim, S. W. Seo, D. H. Kim, K. Zhu, T. Park, J. Y. J. S. Kim, *ChemSusChem* **2017**, *10*, 2660.

[53] M. Bonomo, D. Dini, A. G. Marrani, *Langmuir* **2016**, *32*, 11540.

[54] N. Pant, A. Kulkarni, M. Yanagida, Y. Shirai, T. Miyasaka, K. Miyano, *Adv. Mater. Interfaces* **2020**, *7*, 1901748.

[55] M. B. Islam, M. Yanagida, Y. Shirai, Y. Nabetani, K. Miyano, *ACS Omega* **2017**, *2*, 2291.

[56] E. Aydin, J. Troughton, M. De Bastiani, E. Ugur, M. Sajjad, A. Alzahrani, M. Neophytou, U. Schwingenschlögl, F. Laquai, D. Baran, S. De Wolf, *ACS Appl. Energy Mater.* **2018**, *1*, 6227.

[57] N. Phung, M. Verheijen, A. Todinova, K. Datta, M. Verhage, A. Al-Ashouri, H. Köbler, X. Li, A. Abate, S. Albrecht, M. Creatore, *ACS Appl. Mater. Interfaces* **2022**, *14*, 2166.

[58] D. Di Girolamo, N. Phung, M. Jošt, A. Al-Ashouri, G. Chistiakova, J. Li, J. A. Márquez, T. Unold, L. Korte, S. Albrecht, A. Di Carlo, D. Dini, A. Abate, *Adv. Mater. Interfaces* **2019**, *6*, 1900789.

[59] X. Yin, J. Han, Y. Zhou, Y. Gu, M. Tai, H. Nan, Y. Zhou, J. Li, H. Lin, *J. Mater. Chem. A* **2019**, *7*, 5666.

[60] D. Di Girolamo, F. Matteocci, F. U. Kosasih, G. Chistiakova, W. Zuo, G. Divitini, L. Korte, C. Ducati, A. Di Carlo, D. Dini, A. Abate, *Adv. Energy Mater.* **2019**, *9*, 1901642.

[61] Y. Hu, Z. Yang, X. Cui, P. Zeng, F. Li, X. Liu, G. Feng, M. Liu, *ACS Appl. Mater. Interfaces* **2022**, *14*, 13431.

[62] C. C. Boyd, R. C. Shallcross, T. Moot, R. Kerner, L. Bertoluzzi, A. Onno, S. Kavadiya, C. Chosy, E. J. Wolf, J. Werner, J. A. Raiford, C. de Paula, A. F. Palmstrom, Z. J. Yu, J. J. Berry, S. F. Bent, Z. C. Holman, J. M. Luther, E. L. Ratcliff, N. R. Armstrong, M. D. McGehee, *Joule* **2020**, *4*, 1759.

[63] S. Zhumagali, F. H. Isikgor, P. Maity, J. Yin, E. Ugur, M. De Bastiani, A. S. Subbiah, A. J. Mirabelli, R. Azmi, G. T. Harrison, J. Troughton, E. Aydin, J. Liu, T. Allen, A. ur Rehman, D. Baran, O. F. Mohammed, S. De Wolf, *Adv. Energy Mater.* **2021**, *11*, 2101662.

[64] J. Zhang, J. Long, Z. Huang, J. Yang, X. Li, R. Dai, W. Sheng, L. Tan, Y. Chen, *Chem. Eng. J.* **2021**, *426*, 131357.

[65] A. Al-Ashouri, A. Magomedov, M. Roß, M. Jošt, M. Talaikis, G. Chistiakova, T. Bertram, J. A. Márquez, E. Köhnen, E. Kasparavičius, S. Levcenco, L. Gil-Escrig, C. J. Hages, R. Schlatmann, B. Rech, T. Malinauskas, T. Unold, C. A. Kaufmann, L. Korte, G. Niaura, V. Getautis, S. Albrecht, *Energy Environ. Sci.* **2019**, *12*, 3356.

[66] M. Roß, L. Gil-Escrig, A. Al-Ashouri, P. Tockhorn, M. Jošt, B. Rech, S. Albrecht, *ACS Appl. Mater. Interfaces* **2020**, *12*, 39261.

[67] M. Ebert, H. Stascheit, I. Hädrich, U. Eitner, The Impact of Angular Dependent Loss Measurement on PV Module Energy Yield Prediction.

[68] A. R. M. Alghamdi, M. Yanagida, Y. Shirai, G. G. Andersson, K. Miyano, *ACS Omega* **2022**, *7*, 12147.

[69] M. A. Ruiz-Preciado, F. Gota, P. Fassl, I. M. Hossain, R. Singh, F. Laufer, F. Schackmar, T. Feeney, A. Farag, I. Allegro, H. Hu, S. Gharibzadeh, B. A. Nejand, V. S. Gevaerts, M. Simor, P. J. Bolt, U. W. Paetzold, *ACS Energy Lett.* **2022**, *7*, 2273.

[70] L. Li, Y. Wang, X. Wang, R. Lin, X. Luo, Z. Liu, K. Zhou, S. Xiong, Q. Bao, G. Chen, Y. Tian, Y. Deng, K. Xiao, J. Wu, M. I. Saidaminov, H. Lin, C. Q. Ma, Z. Zhao, Y. Wu, L. Zhang, H. Tan, *Nat. Energy* **2022**, *7*, 177.

[71] P. Caprioglio, C. M. Wolff, O. J. Sandberg, A. Armin, B. Rech, S. Albrecht, D. Neher, M. Stolterfoht, *Adv. Energy Mater.* **2020**, *10*, 2000502.

[72] P. Fassl, V. Lami, F. J. Berger, L. M. Falk, J. Zaumseil, B. S. Richards, I. A. Howard, Y. Vaynzof, U. W. Paetzold, *Matter* **2021**, *4*, 1391.

[73] S. Gharibzadeh, B. Abdollahi Nejand, M. Jakoby, T. Abzieher, D. Hauschild, S. Moghadamzadeh, J. A. Schwenzer, P. Brenner, R. Schmager, A. A. Haghighirad, L. Weinhardt, U. Lemmer, B. S. Richards, I. A. Howard, U. W. Paetzold, *Adv. Energy Mater.* **2019**, *9*, 1803699.

[74] M. Saliba, T. Matsui, J.-Y. Y. Seo, K. Domanski, J.-P. P. Correa-Baena, M. K. Nazeeruddin, S. M. Zakeeruddin, W. Tress, A. Abate, A. Hagfeldt, M. Grätzel, *Energy Environ. Sci.* **2016**, *9*, 1989.

[75] M. Saliba, J. P. Correa-Baena, C. M. Wolff, M. Stolterfoht, N. Phung, S. Albrecht, D. Neher, A. Abate, *Chem. Mater.* **2018**, *30*, 4193.

[76] S. Ghosh, S. Mishra, T. Singh, *Adv. Mater. Interfaces* **2020**, *7*, 2000950.

[77] S. Chen, X. Xiao, B. Chen, L. L. Kelly, J. Zhao, Y. Lin, M. F. Toney, J. Huang, *Sci. Adv.* **2021**, *7*, 2412.

[78] S. Chen, X. Dai, S. Xu, H. Jiao, L. Zhao, J. Huang, *Science* **2021**, *373*, 902.

[79] C. Liu, Y.-B. Cheng, Z. Ge, *Chem. Soc. Rev.* **2020**, *49*, 1653.

[80] A. Farag, R. Schmager, P. Fassl, P. Noack, B. Wattenberg, T. Dippell, U. W. Paetzold, *ACS Appl. Energy Mater.* **2022**, *5*, 6700.

[81] L. Wagner, P. Schygulla, J. P. Herterich, M. Elshamy, D. Bogachuk, S. Zouhair, S. Mastroianni, U. Würfel, Y. Liu, S. M. Zakeeruddin, M. Grätzel, A. Hinsch, S. W. Glunz, *Matter* **2022**, *5*, 2352.

[82] E. M. Tennyson, K. Frohna, W. K. Drake, F. Sahli, T. Chien-Jen Yang, F. Fu, J. Werner, C. Chosy, A. R. Bowman, T. A. S. Doherty, Q. Jeangros, C. Ballif, S. D. Stranks, *ACS Energy Lett.* **2021**, *6*, 2293.

[83] G. Seo, D. Lee, S. Heo, M. Seol, Y. Lee, K. Kim, S. H. Kim, J. Lee, D. Lee, J. Lee, D. W. Kwak, D. Lee, H. Y. Cho, J. Park, T. K. Ahn, M. K. Nazeeruddin, *ACS Energy Lett.* **2017**, *2*, 1705.

[84] F. Fu, S. Pisoni, Q. Jeangros, J. Sastre-Pellicer, M. Kawecki, A. Paracchino, T. Moser, J. Werner, C. Andres, L. Duchêne, P. Fiala, M. Rawlence, S. Nicolay, C. Ballif, A. N. Tiwari, S. Buecheler, *Energy Environ. Sci.* **2019**, *12*, 3074.

[85] S. Liu, Y. Guan, Y. Sheng, Y. Hu, Y. Rong, A. Mei, H. Han, *Adv. Energy Mater.* **2020**, *10*, 1902492.

[86] J. Wang, G. Jin, Q. Zhen, C. He, Y. Duan, J. Wang, G. Jin, Y. Duan, C. He, Q. Zhen, *Adv. Mater. Interfaces* **2021**, *8*, 2002078.

[87] F. Zhang, K. Zhu, *Adv. Energy Mater.* **2020**, *10*, 1902579.

[88] E. Aydin, M. Bastiani, S. Wolf, *Adv. Mater.* **2019**, *31*, 1900428.

[89] H. Wang, Z. Wang, Z. Yang, Y. Xu, Y. Ding, L. Tan, C. Yi, Z. Zhang, K. Meng, G. Chen, Y. Zhao, Y. Luo, X. Zhang, A. Hagfeldt, J. Luo, *Adv. Mater.* **2020**, *32*, 2000865.

[90] T. J. Jacobsson, J. P. Correa-Baena, E. Halvani Anaraki, B. Philippe, S. D. Stranks, M. E. F. Bouduban, W. Tress, K. Schenk, J. Teuscher, J. E. Moser, H. Rensmo, A. Hagfeldt, *J. Am. Chem. Soc.* **2016**, *138*, 10331.

[91] B. Park, N. Kedem, M. Kulbak, D. Y. Lee, W. S. Yang, N. J. Jeon, J. Seo, G. Kim, K. J. Kim, T. J. Shin, G. Hodes, D. Cahen, S. Il Seok, *Nat. Commun.* **2018**, *9*, 3301.

[92] F. Liu, Q. Dong, M. K. Wong, A. B. Djurišić, A. Ng, Z. Ren, Q. Shen, C. Surya, W. K. Chan, J. Wang, A. M. C. Ng, C. Liao, H. Li, K. Shih, C. Wei, H. Su, J. Dai, *Adv. Energy Mater.* **2016**, *6*, 1502206.

[93] Y. C. Kim, N. J. Jeon, J. H. Noh, W. S. Yang, J. Seo, J. S. Yun, A. Ho-Baillie, S. Huang, M. A. Green, J. Seidel, T. K. Ahn, S. Il Seok, *Adv. Energy Mater.* **2016**, *6*, 1502104.

[94] G. Tumen-Ulzii, C. Qin, D. Klotz, M. R. Leyden, P. Wang, M. Auffray, T. Fujihara, T. Matsushima, J.-W. Lee, S.-J. Lee, Y. Yang, C. Adachi, G. Tumen-Ulzii, C. Qin, M. R. Leyden, M. Auffray, C. Adachi, D. Klotz, T. Matsushima, P. Wang, T. Fujihara, J. Lee, S. Lee, Y. Yang, *Adv. Mater.* **2020**, *32*, 1905035.

[95] Z. Hu, Q. An, H. Xiang, L. Aigouy, B. Sun, Y. Vaynzof, Z. Chen, *ACS Appl. Mater. Interfaces* **2020**, *12*, 54824.

[96] T. Meier, T. P. Gujar, A. Schönleber, S. Olthof, K. Meerholz, S. van Smaalen, F. Panzer, M. Thelakkat, A. Köhler, *J. Mater. Chem. C* **2018**, *6*, 7512.

[97] A. Merdasa, A. Kiligaridis, C. Rehermann, M. Abdi-Jalebi, J. Stöber, B. Louis, M. Gerhard, S. D. Stranks, E. L. Unger, I. G. Scheblykin, *ACS Energy Lett.* **2019**, *4*, 1370.

[98] P. Fassl, V. Lami, A. Bausch, Z. Wang, M. T. Klug, H. J. Snaith, Y. Vaynzof, *Energy Environ. Sci.* **2018**, *11*, 3380.

[99] P. Fassl, Y. Zakharko, L. M. Falk, K. P. Goetz, F. Paulus, A. D. Taylor, J. Zaumseil, Y. Vaynzof, *J. Mater. Chem. C* **2019**, *7*, 5285.

[100] J. Barbé, M. Newman, S. Lilliu, V. Kumar, H. K. H. Lee, C. Charbonneau, C. Rodenburg, D. Lidzey, W. C. Tsoi, *J. Mater. Chem. A* **2018**, *6*, 23010.

[101] D. H. Cao, C. C. Stoumpos, C. D. Malliakas, M. J. Katz, O. K. Farha, J. T. Hupp, M. G. Kanatzidis, *APL Mater.* **2014**, *2*, 091101.

[102] B. Roose, K. Dey, Y.-H. Chiang, R. H. Friend, S. D. Stranks, *J. Phys. Chem. Lett.* **2020**, *11*, 6505.

[103] M. Jiang, Y. Wu, Y. Zhou, Z. Wang, *AIP Adv.* **2019**, *9*, 085301.

[104] D. Bi, W. Tress, M. I. Dar, P. Gao, J. Luo, C. Renevier, K. Schenk, A. Abate, F. Giordano, J.-P. C. Baena, J.-D. Decoppet, S. M. Zakeeruddin, M. K. Nazeeruddin, M. Grätzel, A. Hagfeldt, *Sci. Adv.* **2016**, *2*, e1501170.

[105] W. S. Yang, B. W. Park, E. H. Jung, N. J. Jeon, Y. C. Kim, D. U. Lee, S. S. Shin, J. Seo, E. K. Kim, J. H. Noh, S. Il Seok, *Science* **2017**, *356*, 1376.

[106] S. Thampy, W. Xu, J. W. P. Hsu, *J. Phys. Chem. Lett.* **2021**, *12*, 8495.

[107] S. Thampy, B. Zhang, K.-H. Hong, K. Cho, J. W. P. Hsu, *ACS Energy Lett.* **2020**, *5*, 1147.

[108] D. Głowienka, D. Zhang, F. Di Giacomo, M. Najafi, S. Veenstra, J. Szmytkowski, Y. Galagan, *Nano Energy* **2020**, *67*, 104186.

[109] S. Tan, I. Yavuz, M. H. Weber, T. Huang, C. H. Chen, R. Wang, H. C. Wang, J. H. Ko, S. Nuryyeva, J. Xue, Y. Zhao, K. H. Wei, J. W. Lee, Y. Yang, *Joule* **2020**, *4*, 2426.

[110] C. Besleaga, L. E. Abramiuc, V. Stancu, A. G. Tomulescu, M. Sima, L. Trinca, N. Plugaru, L. Pintilie, G. A. Nemnes, M. Iliescu, H. G. Svavarsson, A. Manolescu, I. Pintilie, *J. Phys. Chem. Lett.* **2016**, *7*, 5168.

[111] W. Q. Wu, P. N. Rudd, Z. Ni, C. H. Van Brackle, H. Wei, Q. Wang, B. R. Ecker, Y. Gao, J. Huang, *J. Am. Chem. Soc.* **2020**, *142*, 3989.

[112] B. Chen, S. W. Baek, Y. Hou, E. Aydin, M. De Bastiani, B. Scheffel, A. Proppe, Z. Huang, M. Wei, Y. K. Wang, E. H. Jung, T. G. Allen, E. Van Kerschaver, F. P. García de Arquer, M. I. Saidaminov, S. Hoogland, S. De Wolf, E. H. Sargent, *Nat. Commun.* **2020**, *11*, 1257.

[113] Y. Lv, H. Zhang, J. Wang, L. Chen, L. Bian, Z. An, Z. Qian, G. Ren, J. Wu, F. Nüesch, W. Huang, *Research* **2020**, *2020*, 2763409.

[114] J. W. Lee, H. S. Kim, N. G. Park, *Acc. Chem. Res.* **2016**, *49*, 311.

[115] L. Zhu, Y. Xu, P. Zhang, J. Shi, Y. Zhao, H. Zhang, J. Wu, Y. Luo, D. Li, Q. Meng, *J. Mater. Chem. A* **2017**, *5*, 20874.

[116] D. Zheng, T. Pauporté, *J. Mater. Chem. A* **2021**, *9*, 17801.

[117] P. Dally, D. Messou, M. Robillard, S. Cacovich, A. Yaiche, J. Rousset, A. Etcheberry, M. Bouttemy, presented at IEEE Photovoltaic Spec. Conf., 48th Fort Lauderdale, FL **2021**.

[118] F. M. Rombach, S. A. Haque, T. J. Macdonald, *Energy Environ. Sci.* **2021**, *14*, 5161.

[119] M. A. Mahmud, J. Zheng, S. Tang, G. Wang, J. Bing, A. D. Bui, J. Qu, L. Yang, C. Liao, H. Chen, S. P. Bremner, H. T. Nguyen, J. Cairney, A. W. Y. Ho-Baillie, *Adv. Energy Mater.* **2022**, *12*, 2201672.

[120] N. Liu, L. Wang, F. Xu, J. Wu, T. Song, Q. Chen, *Front Chem* **2020**, *8*, 8.

[121] F. Fu, S. Pisoni, Q. Jeangros, J. Sastre-Pellicer, M. Kawecki, A. Paracchino, T. Moser, J. Werner, C. Andres, L. Duchêne, P. Fiala, M. Rawlence, S. Nicolay, C. Ballif, A. N. Tiwari, S. Buecheler, *Energy Environ. Sci.* **2019**, *12*, 3074.

[122] R. Wang, J. Xue, X. Chen, C. Yao, Z. K. Wang, M. H. Weber, A. H. Rose, S. Nuryyeva, J. Zhu, T. Huang, Y. Zhao, S. Tan, M. C. Beard, Y. Yan, K. Zhu, Y. Yang, *Matter* **2021**, *4*, 2417.

[123] J. Ye, G. Liu, L. Jiang, H. Zheng, L. Zhu, X. Zhang, H. Wang, X. Pan, S. Dai, *Appl. Surf. Sci.* **2017**, *407*, 427.

[124] J. Zhao, Y. Deng, H. Wei, X. Zheng, Z. Yu, Y. Shao, J. E. Shield, J. Huang, *Sci. Adv.* **2017**, *3*, eaao5616.

[125] K. A. Bush, N. Rolston, A. Gold-Parker, S. Manzoor, J. Hausele, Z. J. Yu, J. A. Raiford, R. Cheacharoen, Z. C. Holman, M. F. Toney, R. H. Dauskardt, M. D. McGehee, *ACS Energy Lett.* **2018**, *3*, 1225.

[126] M. Dailey, Y. Li, A. D. Printz, *ACS Omega* **2021**, *6*, 30214.

[127] U. D. Menda, G. Ribeiro, D. Nunes, T. Calmeiro, H. Águas, E. Fortunato, R. Martins, M. J. Mendes, *Mater. Adv.* **2021**, *2*, 6344.

[128] A. Bercegol, F. J. Ramos, A. Rebai, T. Guillemot, J.-B. Puel, J.-F. Guillemoles, D. Ory, J. Rousset, L. Lombez, *J. Phys. Chem. C* **2018**, *122*, 23345.

[129] S.-G. Kim, J. Kim, P. Ramming, Y. Zhong, K. Schötz, S. J. Kwon, S. Huettner, F. Panzer, N. Park, *Nat. Commun.* **2021**, *12*, 1554.

[130] K. Sveinbjörnsson, K. Aitola, J. Zhang, M. B. Johansson, X. Zhang, J.-P. Correa-Baena, A. Hagfeldt, G. Boschloo, E. M. J. Johansson, *J. Mater. Chem. A* **2016**, *4*, 16536.

[131] C. Zhu, X. Niu, Y. Fu, N. Li, C. Hu, Y. Chen, X. He, G. Na, P. Liu, H. Zai, Y. Ge, Y. Lu, X. Ke, Y. Bai, S. Yang, P. Chen, Y. Li, M. Sui, L. Zhang, H. Zhou, Q. Chen, *Nat. Commun.* **2019**, *10*, 101.

[132] S. Braunger, L. E. Mundt, C. M. Wolff, M. Mews, C. Rehermann, M. Jošt, A. Tejada, D. Eisenhauer, C. Becker, J. A. Guerra, E. Unger, L. Korte, D. Neher, M. C. Schubert, B. Rech, S. Albrecht, *J. Phys. Chem. C* **2018**, *122*, 17123.

[133] L. Chao, T. Niu, W. Gao, C. Ran, L. Song, Y. Chen, W. Huang, L. Chao, T. Niu, W. Gao, C. Ran, L. Song, W. Huang, Y. Chen, *Adv. Mater.* **2021**, *33*, 2005410.

**ADVANCED
SCIENCE NEWS**

www.advancedsciencenews.com

**ADVANCED
FUNCTIONAL
MATERIALS**

www.afm-journal.de

[134] Y.-H. Seo, E.-C. Kim, S.-P. Cho, S.-S. Kim, S.-I. Na, *Appl. Mater. Today* **2017**, *9*, 598.

[135] B. Cai, W. H. Zhang, J. Qiu, *Chinese J. Catal.* **2015**, *36*, 1183.

[136] J. Li, J. Dagar, O. Shargaieva, M. A. Flatken, H. Köbler, M. Fenske, C. Schultz, B. Stegemann, J. Just, D. M. Többens, A. Abate, R. Munir, E. Unger, *Adv. Energy Mater.* **2021**, *11*, 2003460.

[137] J. Zhao, Y. Deng, H. Wei, X. Zheng, Z. Yu, Y. Shao, J. E. Shield, J. Huang, *Sci. Adv.* **2017**, *3*, 5616.

[138] J. Wu, S. C. Liu, Z. Li, S. Wang, D. J. Xue, Y. Lin, J. S. Hu, *Natl Sci Rev* **2021**, *8*, 2021.

[139] E. Gutierrez-Partida, H. Hempel, S. Caicedo-Dávila, M. Raoufi, F. Peña-Camargo, M. Grischek, R. Gunder, J. Diekmann, P. Caprioglio, K. O. Brinkmann, H. Köbler, S. Albrecht, T. Riedl, A. Abate, D. Abou-Ras, T. Unold, D. Neher, M. Stolterfoht, *ACS Energy Lett.* **2021**, *6*, 1045.

[140] D. H. Kim, C. P. Muzzillo, J. Tong, A. F. Palmstrom, B. W. Larson, C. Choi, S. P. Harvey, S. Glynn, J. B. Whitaker, F. Zhang, Z. Li, H. Lu, M. F. A. M. van Hest, J. J. Berry, L. M. Mansfield, Y. Huang, Y. Yan, K. Zhu, *Joule* **2019**, *3*, 1734.

[141] M. Stolterfoht, C. M. Wolff, J. A. Márquez, S. Zhang, C. J. Hages, D. Rothhardt, S. Albrecht, P. L. Burn, P. Meredith, T. Unold, D. Neher, *Nat. Energy* **2018**, *3*, 847.

[142] F. Peña-Camargo, P. Caprioglio, F. Zu, E. Gutierrez-Partida, C. M. Wolff, K. Brinkmann, S. Albrecht, T. Riedl, N. Koch, D. Neher, M. Stolterfoht, *ACS Energy Lett.* **2020**, *5*, 2728.

[143] A. B. Morales-Vilches, E.-C. Wang, T. Henschel, M. Kubicki, A. Cruz, S. Janke, L. Korte, R. Schlatmann, B. Stannowski, *Phys. status solidi* **2020**, *217*, 1900518.

[144] B. Abdollahi Nejand, D. B. Ritzer, H. Hu, F. Schackmar, S. Moghadamzadeh, T. Feeney, R. Singh, F. Laufer, R. Schmager, R. Azmi, M. Kaiser, T. Abzieher, S. Gharibzadeh, E. Ahlswede, U. Lemmer, B. S. Richards, U. W. Paetzold, *Nat. Energy* **2022**, *7*, 620.

[145] W. Witte, W. Hempel, S. Paetel, R. Menner, D. Hariskos, *ECS J. Solid State Sci. Technol.* **2021**, *10*, 055006.

[146] J. C. de Mello, H. F. Wittmann, R. H. Friend, *Adv. Mater.* **1997**, *9*, 230.

[147] L. Krückemeier, U. Rau, M. Stolterfoht, T. Kirchartz, *Adv. Energy Mater.* **2020**, *10*, 1902573.

[148] F. Schackmar, H. Eggers, M. Frericks, B. S. Richards, U. Lemmer, G. Hernandez-Sosa, U. W. Paetzold, *Adv. Mater. Technol.* **2021**, *6*, 2000271.